aerospace

MDPI

Article

Effect of Spanwise Dynamic Micro-Vortex Generators on Hypersonic Shock Wave/Turbulent Boundary Layer Interaction

Xiaohui Li *, Hongliang Xiong, Zhan Huang, Hongwei Wang and Shaojie Ren

China Academy of Aerospace Aerodynamics, Beijing 100074, China
* Correspondence: chenxiyue@caaa-spacechina.cn

Abstract

The shock wave/boundary layer interaction (SWBLI) is a common flow phenomenon in high-speed aircraft flow fields. It is important to control the separation caused by SWBLI. This paper investigates the influence of spanwise periodic-motion micro-vortex generators (MVGs) on SWBLI. A combination of particle image velocimetry (PIV), high-frequency Schlieren and fluorescent oil-film visualization was employed to analyze the interaction region of a flat plate compression ramp model. The incoming flow Mach number was 6, and the MVGs oscillation frequencies were 10 Hz, 30 Hz and 50 Hz, respectively. The results reveal that neither the presence nor the spanwise oscillation in the MVGs fundamentally altered the separation–reattachment flow structure. Nonetheless, both factors contributed to an increase in boundary layer thickness and an expansion of the absolute size of the separation region. The trailing vortices generated by the MVGs exerted a stabilizing influence on near-wall turbulent structures, resulting in a reduction in surface friction drag. However, the drag reduction effect diminished as the oscillation frequency increased, corresponding to a weakening of the trailing vortex strength. Additionally, the MVGs and their spanwise oscillation modulated the low-frequency energy distribution of the flow, amplifying the low-frequency oscillation peak associated with the separation shock and raising the time-averaged oscillation position.

Keywords: micro-vortex generators; spanwise oscillation; flow separation; low-frequency oscillation; shock wave/boundary interaction

1. Introduction

Shock wave/boundary-layer interaction (SWBLI) is a complex flow phenomenon commonly observed in the internal and external flows of supersonic and hypersonic vehicles. It can induce flow separation, cause distortions in the flowfield, and lead to a reduction in the total pressure recovery coefficient [1–3]. Additionally, SWBLI can induce unsteady oscillations in the flowfield, resulting in excessive local aerodynamic forces and heat fluxes, which may lead to the unstart of air-breathing engine inlets [4]. Therefore, the effective control of SWBLI is crucial for ensuring the safe and stable operation of high-speed vehicles.

MVGs, as a passive flow control method, are commonly used to induce streamwise vortices by arranging structures such as delta shapes, ribs, wedges, or ramps on the wall surface. Such streamwise vortices effectively enhance momentum exchange between the boundary layer and free stream, thereby suppressing flow separation, improving aerodynamic lift–drag performance, and optimizing heat transfer characteristics. In the 1960s, Schubauer and Spangenberg [5] systematically investigated the mechanism by which

Check for updates

Academic Editor: Tze How New

Received: 30 April 2026
Revised: 12 June 2026
Accepted: 22 June 2026
Published: 29 June 2026

Copyright: © 2026 by the authors. Licensee MDPI, Basel, Switzerland. This article is an open access article distributed under the terms and conditions of the Creative Commons Attribution (CC BY) license.

vortex generators enhance momentum mixing within boundary layers through the generation of streamwise vortices, thereby revealing the fundamental principle underlying boundary layer separation control using vortex generators. Meanwhile, in a seminal study, Pearcey [6] systematically elucidated the physical mechanism of shock-induced boundary layer separation and its prevention, explicitly highlighting the great potential of vortex generators for mitigating shock-induced separation, and thus laying the theoretical foundation for subsequent research. However, conventional vortex generators can reach a height on the order of the local boundary layer thickness, which, in supersonic and hypersonic flows, leads to non-negligible wave drag and additional aerodynamic heating. To overcome this engineering bottleneck, Lin et al. [7–9] first reported the control effect of small-scale vortex generators on turbulent boundary layer separation and systematically reviewed the research progress of low-profile vortex generators for boundary layer separation control, formally facilitating the extension of MVG applications from subsonic to supersonic and hypersonic regimes. Current research on vortex generators primarily focuses on their intrinsic characteristics [10–12] and control effectiveness [13–16] in SWBLI. For instance, Verma et al. [17] experimentally investigated the influence of various MVG sizes and shapes on oblique SWBLI. The configurations examined included Ashill, Anderson, split-Anderson, trapezoidal, and ramp–vane designs, with MVG heights set at 30% and 50% of the local boundary layer thickness. Their findings indicated that different MVG geometries effectively reduced the separation zone size at a Mach number of 2.05. Similarly, Babinsky et al. [18] explored the control performance of ramp–vane MVGs at Mach 2.5 in a simplified inlet oblique SWBLI scenario. The study demonstrated that MVGs of varying heights yielded comparable control effects; however, larger ramp configurations were associated with increased momentum deficit thickness and a substantial rise in profile drag.

MVGs demonstrate effective flow control primarily under design-specific conditions but exhibit limited efficacy in mitigating flow separation when operating under off-design scenarios. To break through this limitation, recent studies have focused on developing hybrid and dynamic control strategies to optimize MVG control performance. Zhang et al. [19] conducted numerical analyses on the combined effects of ramp-type MVGs and transverse jets. Their investigation into the flow structures associated with this ramp–jet configuration revealed that the wake thickness and flow momentum over the ramp are pivotal factors governing jet penetration capability; specifically, reduced momentum and increased wake thickness facilitate enhanced jet penetration. However, this study did not assess the hybrid control method's effectiveness in suppressing flow separation. Zhao et al. [20] examined the control mechanisms and flow-field structures of dynamic MVGs (Dy-MVGs) in supersonic SWBLI at a Ma = 4. The findings indicated that the downstream movement of the MVGs at certain velocities substantially diminishes the localized high-pressure regions induced by shock waves, with greater downstream velocities producing more pronounced control effects. Furthermore, Zhao et al. [21] investigated the application of normal-direction oscillating Dy-MVGs to control SWBLI at compression ramps under incoming Mach numbers of 2.5 and 3.5. The results demonstrated that Dy-MVGs attenuate the strength of separation shocks within the interaction zone, amplify fluctuating pressure and low-frequency energy characteristics, and induce dynamic variations in both the separation shock angle and shock foot position over an extended range. These effects collectively demonstrate the superior control of SWBLI compared to conventional MVGs. Wang et al. [22,23] explored the influence of dynamically oscillating vortex generators, oscillating normally to the wall, on flow separation within supersonic inlets. They observed that the periodic modulation of MVG strength enhances mixing between the boundary layer and the free stream. The oscillatory processes, characterized by

"extrusion" and "suction" effects, continuously energize the airflow, leading to a significant improvement in the velocity distribution within the boundary layer. Consequently, the length of the separation bubble was reduced by 31.76%, and the total pressure recovery coefficient of the inlet was increased.

Nonetheless, it is important to acknowledge that although micro-vortex generators substantially reduce additional drag compared to conventional vortex generators, they still contribute to increased wall friction. Research efforts aimed at mitigating the additional drag induced by vortex generators remain limited. MVGs exert control over flow separation and unsteady shock wave dynamics by generating streamwise vortices that are closely linked to wall flow characteristics. The use of periodically oscillating plates, a technique initially identified by [24], has been shown to reduce wall friction by modifying near-wall flow behavior. Their study revealed that when the lower plate in a channel oscillates periodically at specific frequencies and amplitudes, a significant reduction in wall friction is achieved. Yao et al. [25] conducted numerical investigations into the effects of periodically oscillating plates on compressible channel wall friction at Mach numbers of 0.3, 0.8, and 1.5. They observed that for Mach 0.3 and 0.8, drag reduction initially increased with oscillation period, reached a peak, and subsequently declined. In contrast, at Mach 1.5, drag reduction continued to increase with the oscillation period. Sun et al. [26] explored the influence of spanwise periodically oscillating plates on the flow structure and unsteady characteristics of incident SWBLI. Their findings indicated that spanwise oscillations shift the probability density peak of the angle between streamwise and spanwise shear from 0° to approximately 80–90°, facilitate energy transfer from low-frequency to high-frequency components, and effectively suppress low-frequency motions. Moreover, the penetration height of these spanwise oscillations was approximately 4% of the separation bubble height, thereby exerting minimal impact on the overall flow structure.

Consequently, combining the two control strategies of spanwise oscillation and MVGs, this study proposes a configuration of dynamic MVGs that oscillate periodically in the spanwise direction. Experimental investigations were performed on the SWBLI over a flat plate compression ramp utilizing PIV, fluorescent oil-film visualization, and high-speed Schlieren photography. The influence of spanwise oscillation vortex generators operating at various frequencies on the effects of SWBLI was systematically examined.

2. Experimental Arrangement and Method

2.1. Design of the Spanwise Oscillation MVGs

An oscillatory drive system for a vortex generator was developed, as illustrated in Figure 1. This system primarily consists of an electric motor, a cam and cam bearing assembly, and cross-roller guide rails. The motor actuates the rotation of the camshaft, which in turn produces the periodic spanwise motion of the vortex generator. Operating at a maximum rotational speed of 4000 rpm, the design integrates cross-roller guide rails between the vortex generator and the driving mechanism to substantially minimize resistance during the reciprocating spanwise movements. This optimized arrangement facilitates high-precision spanwise oscillations in the vortex generator by efficiently converting rotational motion into linear displacement while maintaining low frictional losses.

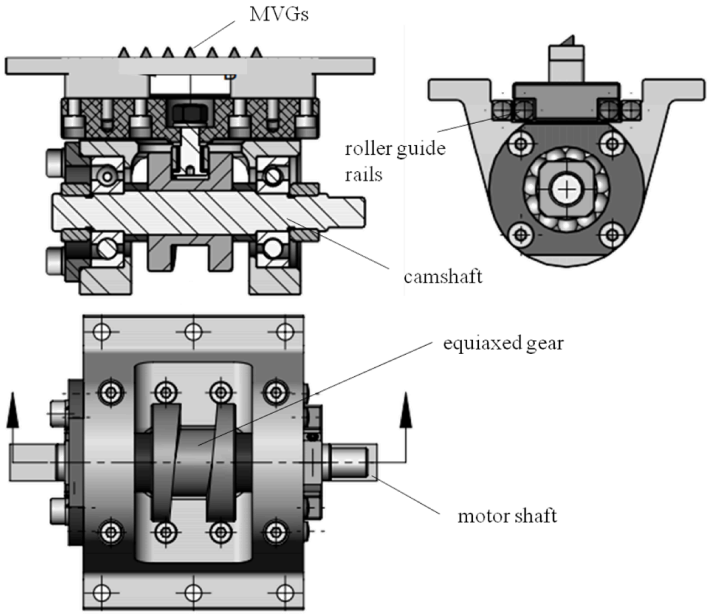

Figure 1. The structure of spanwise oscillation MVGs.

2.2. Experimental Model

As shown in Figure 2, the flat plate had a sharp leading edge to avoid local separation. Its length and width were L = 240 mm and W = 112 mm, respectively. The ramp had a height of 20 mm and a compression angle of 42 degrees to generate a relatively robust strong shock interaction region, and it was positioned 200 mm downstream of the flat-plate leading edge. The vortex generators were designed with a triangular wedge profile, featuring a height of h = 6 mm. The spanwise spacing between two neighboring MVG units was ΔMVG = 9 mm. The dimensionless height was $h/\delta_0 = 0.25$. According to Saad et al. [27] and Wu et al. [28], MVGs with this height can efficiently help the boundary layer to resist reverse pressure gradients, thereby contributing to the flow separation control. The entire array was symmetrically arranged along the spanwise direction and positioned 78 mm downstream from the leading edge of the model. The spanwise oscillation amplitude of MVGs was 3 mm in the experiment.

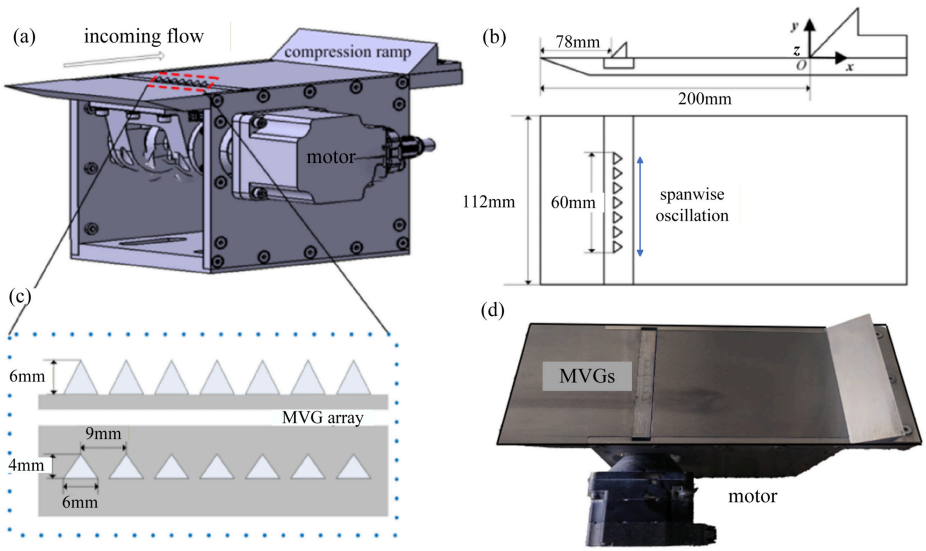

Figure 2. The model's schematic and design parameters. (**a**) Three-dimensional digital model; (**b**) front view and top view; (**c**) the parameter of the MVGs; (**d**) the experimental model.

2.3. Experimental Environment

The experiment was conducted in a hypersonic transient blow-down wind tunnel [29,30] whose cross-section has a size of 170 mm × 170 mm. The maximum duration of the wind tunnel test was 90 s. The side and top of the wind tunnel have optically illuminated windows. The nominal incoming-flow Mach number was set as Ma_∞ = 6, and the total for temperature and pressure was 453 K/2 Mpa. A steel compression ramp model, consisting of a flat plate and a ramp, was placed flush with the nozzle outlet of the wind tunnel. The incoming flow is a turbulent boundary layer with a unit Reynolds number of $\mathrm{Re}_L = 2 \times 10^7\ \mathrm{m}^{-1}$. Table 1 shows the specific experimental methods and conditions. For the spanwise oscillatory motion of the MVGs, the reduced frequency $k = \frac{fL}{U_\infty}$ is further introduced for characterization, where f is the forcing frequency of MVGs, L is a characteristic interaction length, and U_∞ is the freestream velocity.

Table 1. Experimental condition.

Number	Experimental Methods	Experimental Condition	Reduced Frequency
1	PIV	no MVG	/
2	fluorescent oil-film	add MVG	/
3	visualization	f = 10 Hz	0.0007
4	high-speed Schlieren	f = 30 Hz	0.0021
5	photography	f = 50 Hz	0.0033

2.4. Experimental Equipments and Layout

The flow field was experimentally investigated through a combination of particle image velocimetry (PIV), fluorescent oil-film visualization, and high-speed schlieren photography, thereby yielding comprehensive data on the spatial and surface flow characteristics of SWBLI.

(1) PIV

The PIV system employed an SM-CCDB9M17 CCD camera with a spatial resolution of 3388 pixel × 2712 pixel, configured with an inter-frame time of 400 ns and a sampling frequency of 5 Hz. An Nd:YAG high-energy dual-exposure pulsed laser served as the illumination source, operating at a central wavelength of 532 nm with a maximum pulse energy output of 600 mJ. The PIV system employed an CCD camera (B3420, Imperx, Boca Raton, FL USA) with a spatial resolution of 3388 pixel × 2712 pixel, configured with an inter-frame time of ΔT = 400 ns, and a sampling frequency of 5 Hz. A total of 300 valid particle images were acquired, from which 150 instantaneous velocity fields were calculated. These instantaneous fields were then ensemble-averaged to obtain the time–mean velocity field. A Nd:YAG (Vlite-600, Beamtech, Beijing, China) high-energy dual-exposure pulsed laser served as the illumination source, operating at a central wavelength of 532 nm with a maximum pulse energy output of 600 mJ. Titanium dioxide (TiO_2) powder with a nominal diameter of 50 nm was used as tracer particles. Due to particle agglomeration, the effective mean diameter was approximately 200 nm, estimated according to the laboratory environment. The Stokes number of these tracer particles was approximately St = 0.03, below the recommended threshold of St = 0.05 for accurate flow tracking [31]. Figure 3a,b present the front and top views of the PIV measurement arrangement, respectively. The laser sheet illuminates the flow field through the top window of the wind tunnel, and the camera captures images through the side window.

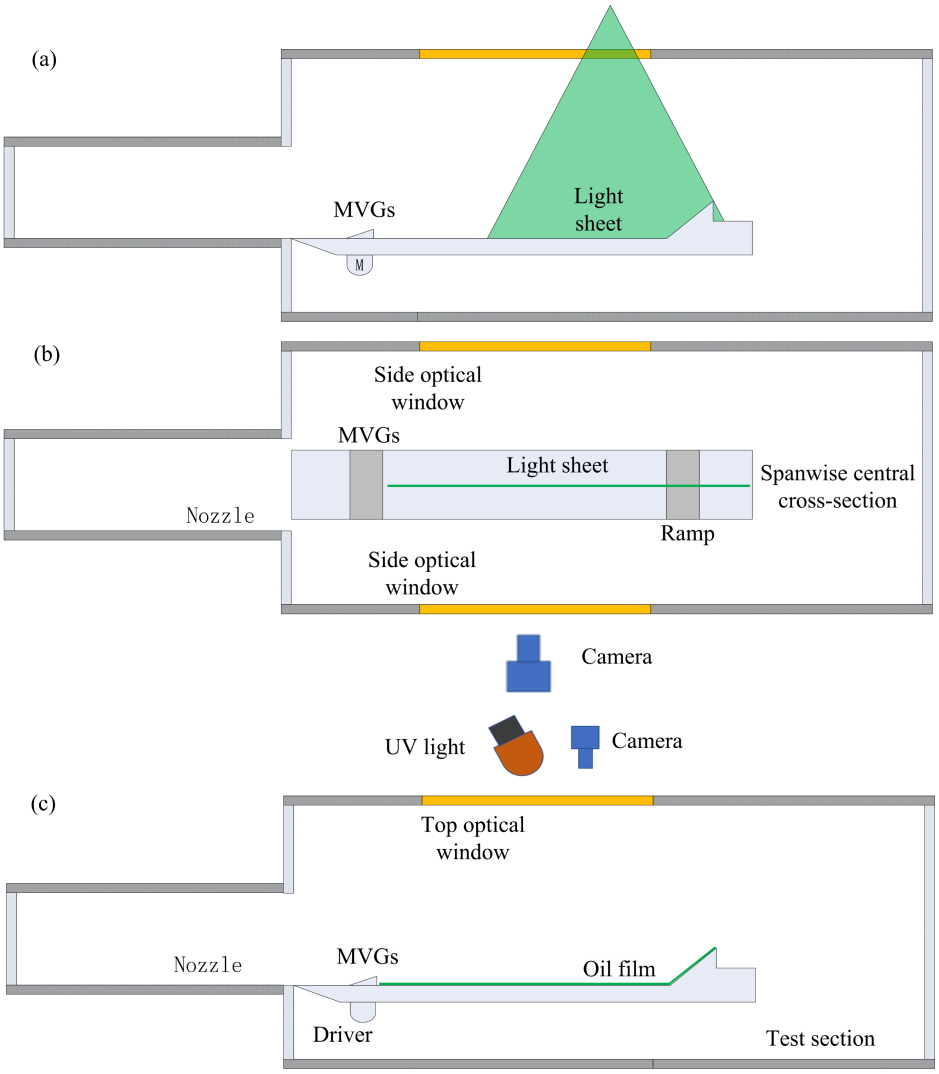

Figure 3. Experimental layout: (**a**) PIV-front view; (**b**) PIV-top view; (**c**) fluorescent oil film.

The measurement uncertainties were evaluated for PIV configurations, primarily considering those arising from camera calibration, straddle time, and velocity fields. The maximum particle offset within the straddle frames is about 9 pixels. The calibration error is ±0.1 pixels, and the corresponding measurement uncertainty is 0.8%. The straddle-frame time control uncertainty of the synchronous controller is ±0.25 ns, corresponding to a measurement uncertainty of 0.083%. The maximum measurement uncertainty for mean velocity was calculated by $\varepsilon_1 = \sigma_u / \sqrt{n}$, in which σ_u is the standard deviation of the normalized velocity fluctuation u/U_∞ and N is the number of uncorrelated snapshots. In the present study, the maximum σ_u in the free stream flow region is 0.018, corresponding to measurement uncertainties 0.15%.

(2) Fluorescent Oil Film

The oil-film measurement apparatus primarily comprised an ultraviolet (UV) illumination subsystem and an imaging unit. The UV light source was emitted at a central wavelength of 365 nm, delivering an irradiance of 14,000 μW/cm^2 at a working distance of 380 mm, while exhibiting excellent scattering uniformity. Temporal intensity fluctuations were constrained to less than 0.03 ms through precise optical modulation. The imaging camera employed was identical to that used in the PIV system, with a sampling frequency of 12 Hz. A total of 300 valid images were acquired with a camera exposure time of 15 ms. Figure 3c presents a schematic of the oil-film measurement arrangement. Both the cam-

era and the light source were placed at the top window of the wind tunnel to provide illumination and capture images.

Since the calculated results are relative skin friction distributions without a true value for reference, the uncertainty of the oil-film method was evaluated using repeated measurement deviations. The main sources of uncertainty in the oil-film measurements originate from the illumination uniformity of the light source and the computational model. Under different test conditions, the same light source intensity and illumination direction were used; therefore, the effect of illumination uniformity is negligible. The computational model mainly involves the temperature-induced change in oil viscosity and the lack of validity of the governing equation due to oil-film thickness variations. The wind tunnel freestream temperature was measured using an SBWR temperature sensor with an accuracy of 0.2%. At a freestream total temperature of 453 K, the resulting temperature deviation is 0.1 K, which has a negligible effect on the oil viscosity. In addition, the oil-film thickness applied on the surface ranged from 40 to 80 μm. Using the mean standard deviation $\varepsilon_2 = \sqrt{\frac{\sum_{i=1}^{n}(|\tau_i|-|\overline{\tau}|)^2}{n-1}}$, in which τ_i is wall shear stress, $\overline{\tau}_i$ is the averaged wall shear stress, and n is the number of experiments, the combined uncertainty of the relative skin friction calculation is better than 3%.

(3) High-Speed Schlieren System

A Z-type **Schlieren** system was used to visualize the unsteady shock motion in the SWBLI region. The sampling rate was 10 kHz, obtained using a high-speed camera (Photron FASTCAM Nova S12, Tokyo, Japan) with a resolution of 1024 pixels × 1024 pixels. In the measurement, 21,821 experimental images were collected and the camera exposure time was 100 μs.

3. Results and Analysis

3.1. Results of PIV

Figure 4 shows the time-averaged velocity contours and streamlines of the experimental cross-section under different flow conditions. As the flow approaches the corner, the velocity becomes negative, indicating flow separation. Notably, the introduction and oscillation of MVGs do not alter the overall flow structure, which maintains a typical separation–reattachment pattern. Table 2 presents the boundary layer thickness under corresponding to the different operating conditions. The introduction of the MVGs results in a substantial increase in boundary layer thickness, whereas variations in spanwise oscillation frequency exert a negligible influence on it.

Table 2. The boundary layer thicknesses.

Condition	Boundary Layer Thickness
no MVGs	24.0 mm
With MVGs	28.6 mm
oscillation frequency f = 10 Hz	29.2 mm
oscillation frequency f = 30 Hz	29.1 mm
oscillation frequency f = 50 Hz	29.2 mm

We aimed to accurately obtain the separation position p_{sep}, where the velocity direction near the wall changes from a positive value to a negative.

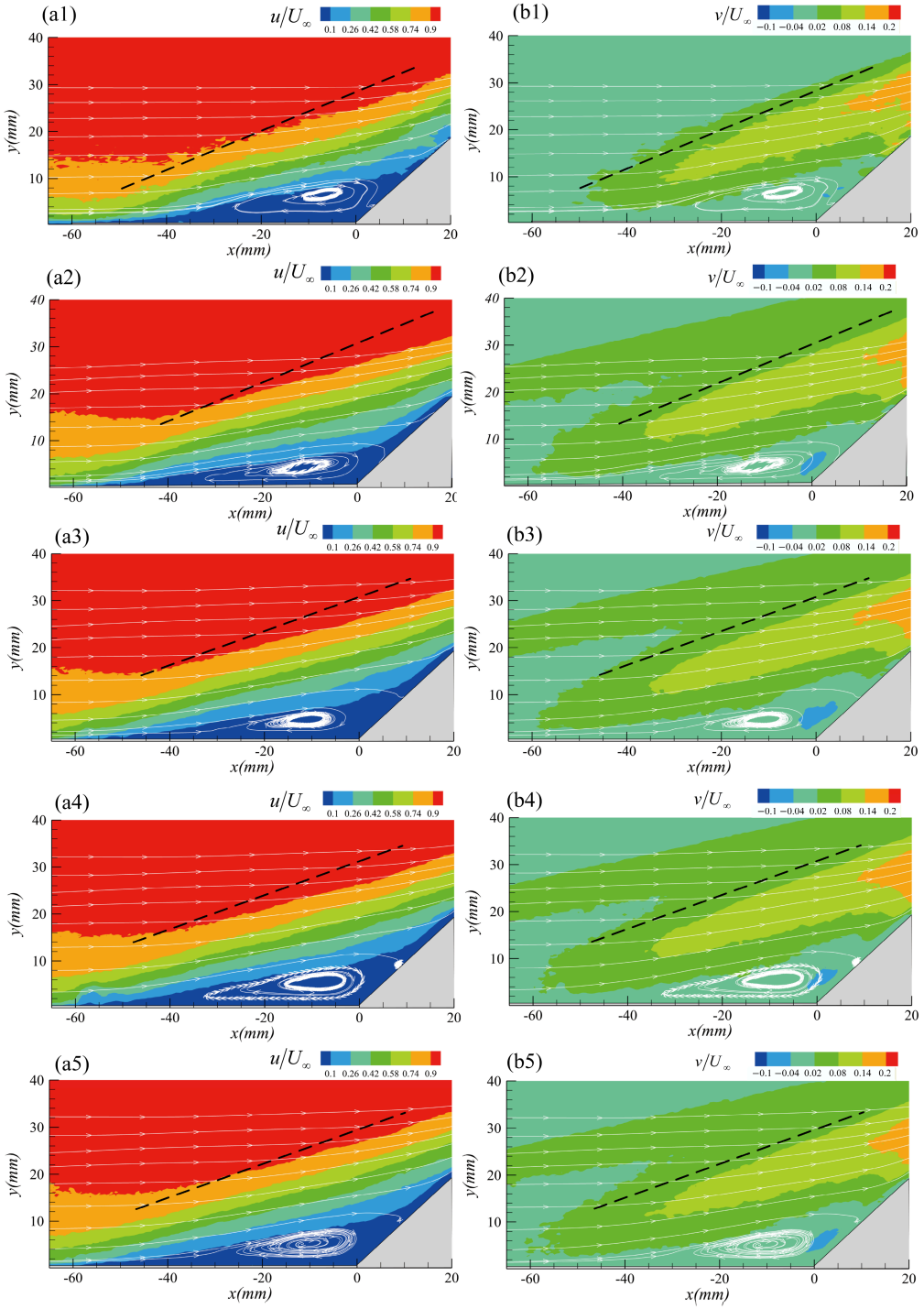

Figure 4. The time-averaged velocity contours and streamline. (**a1**–**a5**) Dimensionless u velocity components, (**b1**–**b5**) dimensionless v velocity components. Rows from top to bottom correspond to the results without MVGs, with MVGs (stationary), and with MVGs oscillating at f = 10 Hz, f = 30 Hz, and f = 50 Hz. The black dashed line denotes the location of the separation shock.

The separation point is primarily determined by a change in streamwise velocity. Taking the freestream direction as a positive, the streamwise velocity remains positive upstream of the separation zone, consistent with the freestream direction. Once the flow enters the separation region, the streamwise velocity reverses and becomes negative. Three consecutive vector points following the separation point are used as verification points to exclude potential erroneous velocity vectors, which must align with the velocity direction

of the separation point. Based on this verification criterion, the positions of the separation point under different conditions can be obtained by Formula (1):

$$p_{sep} = u(x,y) > 0@u(x+1,y) < 0@u(x+2,y) < 0@u(x+3,y) < 0 \quad (1)$$

in which $u(x,y)$ is the streamwise velocity value at position (x,y). To eliminate errors caused by velocity measurements near the wall, the separation point location was determined using the velocity value at $u(x,2)$, as shown in Figure 5, where dis denotes the distance from the separation point to the corner leading edge, and dis/δ_x is non-dimensionalized by the boundary layer thickness under the different conditions of no MVGs, with MVGs, and with spanwise oscillations at frequencies at f = 10 Hz, f = 30 Hz, and f = 50 Hz, respectively. The results show that the introduction of the MVGs results in an upstream shift in the absolute separation point location. Conversely, the spanwise oscillations of the vortex generator exhibit negligible influence on the position of flow separation. Furthermore, dis/δ_x decreased by about 4% and the dis/δ_x remained nearly unchanged at different spanwise oscillation frequencies.

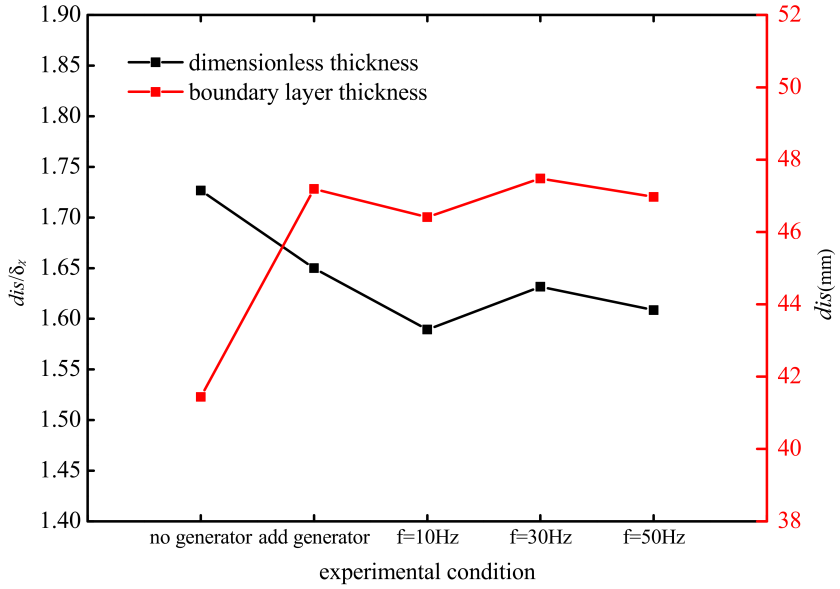

Figure 5. The separation position.

Figure 6a–c show the velocity profiles at x = −60 mm (located in the pre-separation region), x = −40 mm and x = −20 mm (located within the separation region). This shows the velocity profiles becoming increasingly full with the addition of, and oscillations in, the MVGs. These disrupt the striped structure of the turbulent boundary layer, leading to excessive energy dissipation. As a result, the ability to resist separation is further reduced, resulting in an enlargement of the absolute size of the separation zone. Figure 7 compares the shape factor in the range from x = −67 mm to x = −50 mm, denoting the pre-separation region. In the absence of the MVGs, the shape factor H shows minimal variation at locations relatively distant from the separation zone. However, when approaching the separation zone, the shape factor progressively increases due to the intensification of the adverse pressure gradient. Upon the introduction of the MVGs, prior to position $x1$ = −57.8 mm, the shape factor is lower compared to the scenario without the MVGs, suggesting that the wake vortex induced by the MVGs enhances turbulent fluctuations. Beyond position $x1$, the H exceeds that of the case without the MVGs, indicating a reduced capacity to resist flow separation. Furthermore, as the MVGs begin to oscillate, shape factor H correspondingly rises, with the location shifting upstream to $x3$, implying that the spanwise oscillations

in the MVGs diminish the turbulence regularization effect, thereby further reducing the flow's resistance to separation.

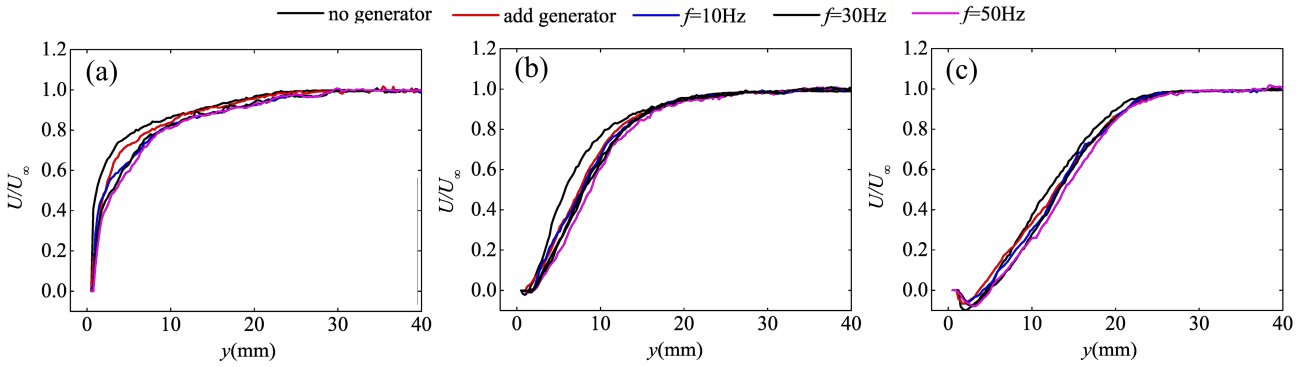

Figure 6. Velocity profile at different positions: (**a**) $x = -60$ mm; (**b**) $x = -40$; (**c**) $x = -20$ mm.

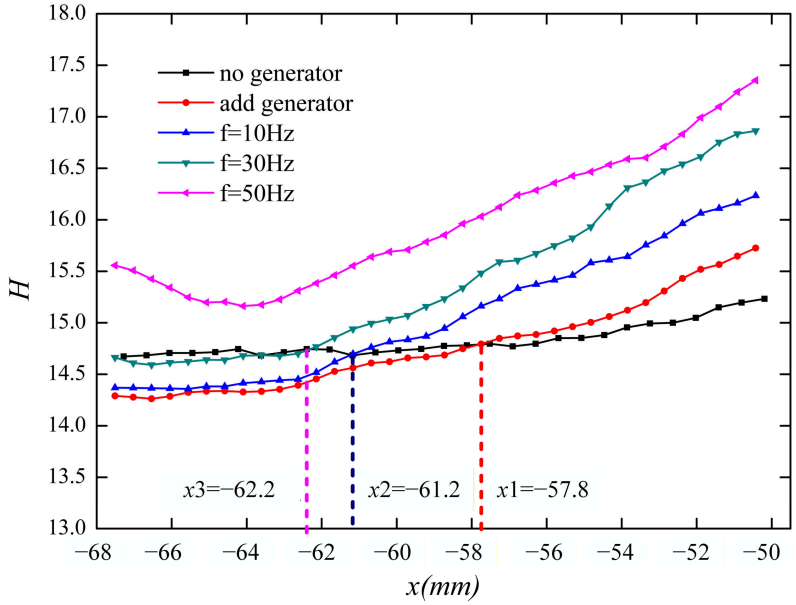

Figure 7. The changes in shape factor, $x1$, $x2$, and $x3$ denote the streamwise positions where the shape factor exceeds that of the case without MVGs, corresponding to added MVGs of 10 Hz and 30 Hz, respectively.

The proper orthogonal decomposition (POD) method [32] was used to conduct a modal analysis of the flowfield. As shown in Figure 8, the cumulative energy of the first five modes approaches 70%, which can be considered the dominant flow modes. Specifically, the first mode accounts for over 40% of the total mode energy, the second mode contributes approximately 10% and the third mode contributes about 5%, while the energy of the remaining modes is below 5%. This indicates that the first three modes can be regarded as the absolute dominant modes governing the flow characteristics. Upon the introduction of the MVGs, the energy contributions of the first and second modes increased. However, as the oscillation frequency increased, the energy contributions of the first and second modes gradually decreased and approached the values observed without MVGs. From the fourth mode onward, the difference in energy contributions became negligible, indicating that the MVGs and oscillation primarily regulate the distribution of low-frequency energy.

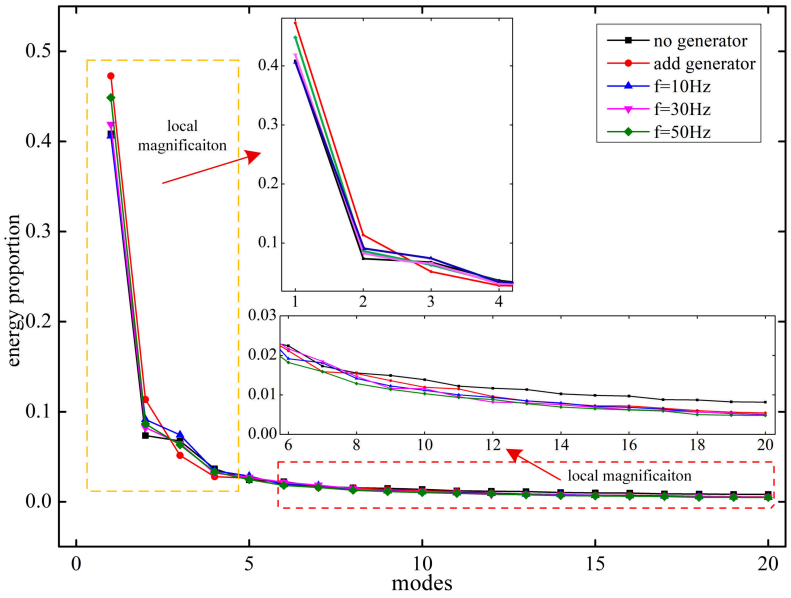

Figure 8. Modal energy percentage of the first 20 modes.

Figure 9 shows a schematic of the interactions in the compression ramp interaction region. Based on the combined Schlieren and PIV results, this indicates the positions of the separation shock, reattachment shock, and separation bubble, and is used to guide the analysis of the dominant energetic structures in the POD modes. Figure 10 shows the pseudo-color maps depicting the first–third-order POD modes of the streamwise velocity under different flow conditions. The results indicate that the flow structures of the first three modes remain similar, suggesting that the MVGs and their spanwise oscillations do not significantly alter the flow structures, which aligns with the results obtained from the PIV. The first mode has the largest energy share and is located inside the separation shock. This is attributed to the unsteadiness of the separation bubble. The second and third modes exhibit alternating positive–negative convective structures. They are nearly identical in shape but spatially phase-shifted. Their energy shares are close to each other, indicating that the second and third modes represent the primary regions of convective flow activity, with similar energies but orthogonal spatial phases. The alternating positive–negative structures are located close to the separation shock and the reattachment shock, respectively, suggesting that they are associated with the unsteadiness of both shocks. Additionally, with the introduction of the MVGs and their spanwise periodic motion, the spatial mode coefficients increase, and the fluctuating region becomes more concentrated.

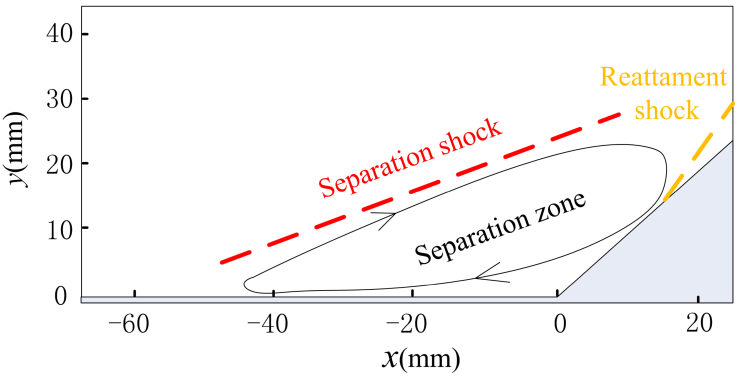

Figure 9. Schematic of the interaction region.

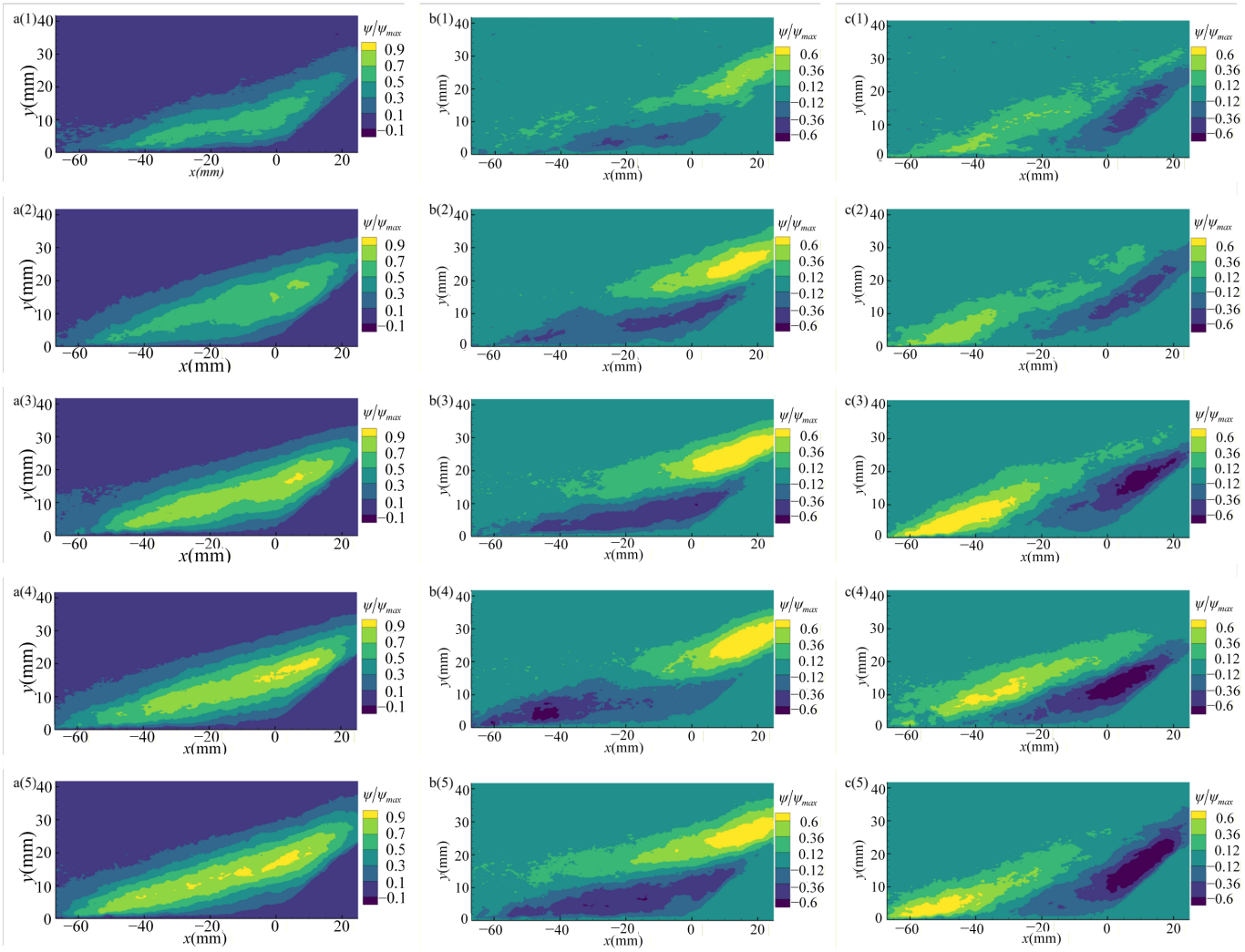

Figure 10. Pseudo-color maps: (**a(1)**–**a(5)**) the first-order POD modes correspond to the results with no MVGs, added MVGs, f = 10 Hz, f = 30 Hz and f = 50 Hz, respectively; (**b(1)**–**b(5)**) the second-order POD modes; (**c(1)**–**c(5)**) the third-order POD modes.

3.2. Results of Fluorescent Oil Film

Figure 11 shows the captured fluorescent oil-flow images. The left portion of the image presents the original field of view, whereas the right portion displays the grayscale-enhanced compression ramp oil-film image, corresponding to the zone enclosed by the blue dashed box in the left half. The relatively low grayscale intensity observed in the compression ramp region of the original image is attributed to the increased entrainment of the oil film by the incoming flow. A clear separation line is discernible within the separation zone. Owing to the limited spanwise expansion effect, the separation line exhibits a "bow-shaped" distribution along the spanwise direction. Compared to the case without MVGs, the presence of MVGs results in an upstream shift in the separation line and a downstream delay of the reattachment line. By comparing Figure 11b–e, it is evident that the spanwise oscillation in the MVGs has negligible impact on the position and morphology of both the separation and reattachment lines, indicating that the spanwise oscillations do not alter the flow structure within the interaction region.

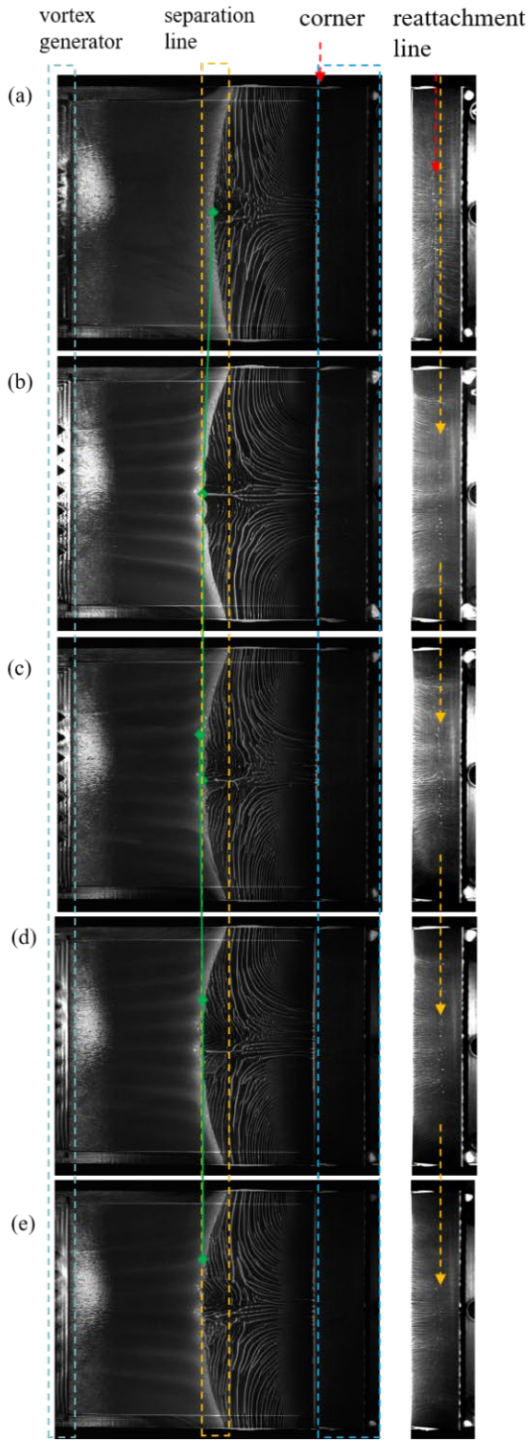

Figure 11. The oil-film images: (**a**) without MVGs; (**b**) with MVGs; (**c**) f = 10 Hz; (**d**) f = 30 Hz; (**e**) f = 50 Hz.

Figure 12 illustrates the distribution of oil-film intensity along the z-direction at $x = -80$ mm. In the absence of MVGs, the oil-film intensity does not exhibit notable periodic variation. However, a distinct periodic pattern emerges in the intensity distribution after the introduction of the MVGs. The regions of higher intensity correspond to the oil-film convergence induced by the trailing vortices of MVGs. The observation indicates that the striped structures characteristic of the turbulent boundary layer are regularized by trailing vortices, thereby reducing their ability to resist boundary layer separation. Following the oscillation in the MVGs, the periodic nature of the oil-film intensity distribution remains

unchanged, but the spanwise intensity fluctuations are reduced. This suggests that the oscillation primarily modifies the anisotropy along the z-direction.

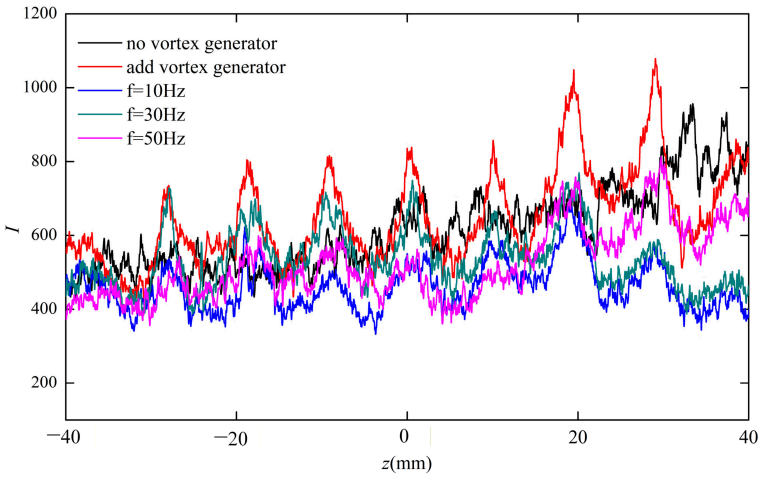

Figure 12. Distribution of spanwise oil-film gray intensity at $x = -80$ mm.

Surface friction drag can be calculated by establishing a relationship between fluorescent intensity and oil-film thickness [33]. Using a variational iteration-based global optical flow computation method [34,35], wall friction drag was calculated to obtain friction drag distributions on the model surface under different oscillation frequencies. It should be noted that the friction drag represents relative values and is not identical to the true friction drag value. Nonetheless, it is suitable for comparative analyses of friction drag variations across different flow conditions. The computational zone is shown in Figure 13.

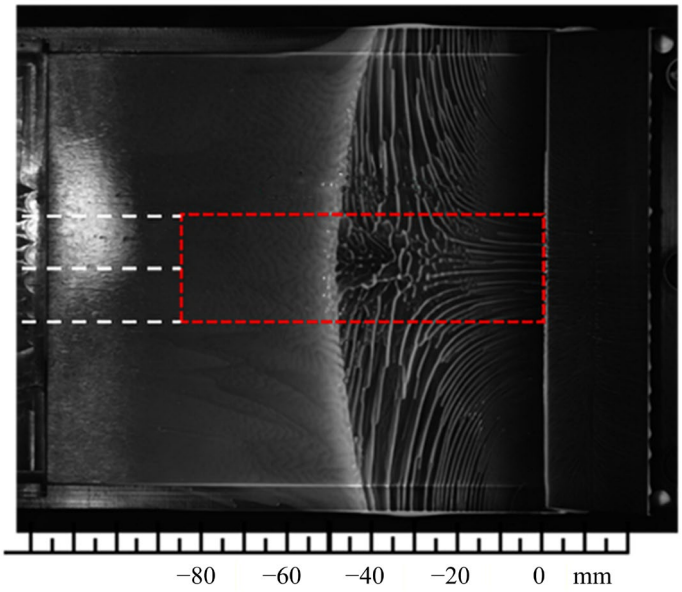

Figure 13. Schematic of the computational domain for surface friction drag. The red dashed box indicates the computational domain, and the white dashed lines show the relative positional relationship between the computable region and the vortex generators.

Figure 14 illustrates the time-averaged surface relative skin friction distribution and streamline patterns. Analysis of the streamlines reveals that the flow is uniformly distributed prior to separation in the absence of MVGs. The introduction of MVGs induces distinct nodal points at the position of the separation line due to the influence of trailing vortices. Simultaneously, the intensified trailing vortices impinge upon the separation line,

forming small-scale vortex structures. Notably, the spanwise-uniform region along the separation line becomes larger after adding MVGs. Subsequent spanwise oscillation in the MVGs results in the near-disappearance of the nodes and the small vortex structures at the separation line are also diminished significantly. This demonstrates that oscillation enhances spanwise flow uniformity, reduces the strength of trailing vortex, and weakens impingement on the separation line. Furthermore, the separation line morphology approaches that observed without MVGs with an increase in the oscillation frequency. From the friction distribution contour, it can be observed that adding MVGs reduces the relative streamwise, spanwise, and total relative surface friction. On the one hand, the suppression of turbulent fluctuations by the organized trailing vortices decreases streamwise friction. On the other hand, the improved spanwise flow uniformity achieved by the MVGs lowers spanwise friction. However, following the oscillation in MVGs, friction increases relative to the stationary MVGs case. As oscillation frequency rises, the relative surfaces friction progressively approaches the values observed without MVGs.

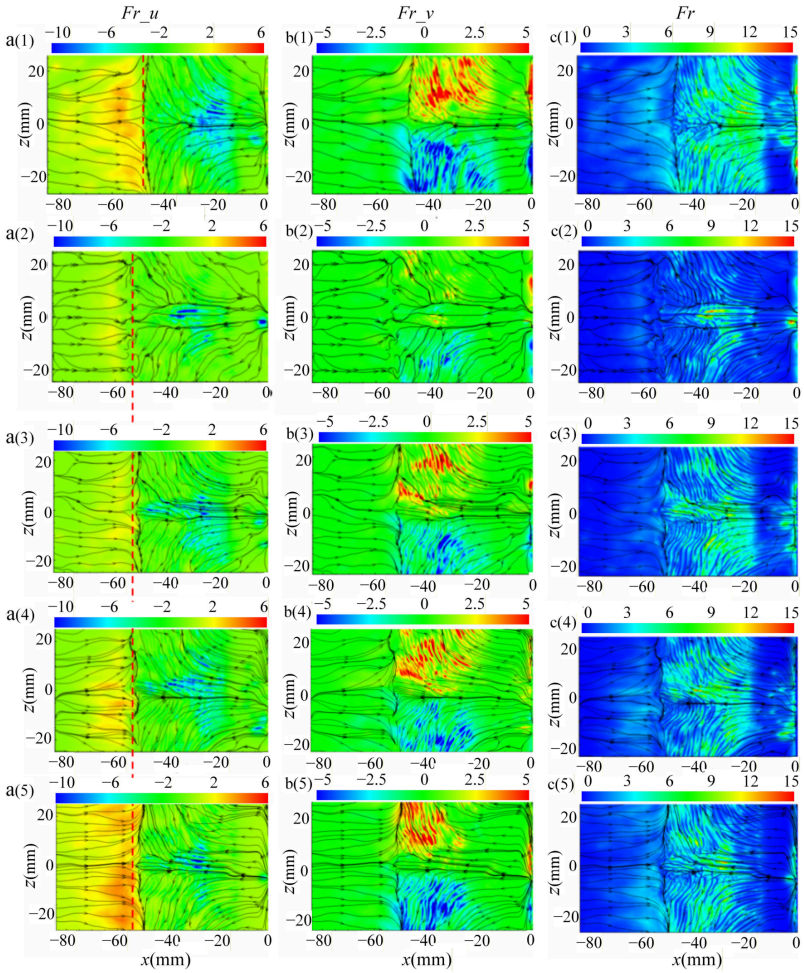

Figure 14. Surface relative friction distribution and streamline patterns: Streamwise (**a(1)–a(5)**), spanwise (**b(1)–b(5)**), and total (**c(1)–c(5)**) relative friction for cases with no MVGs, added MVGs, and with MVG oscillating at f = 10 Hz, f = 30Hz, and f = 50 Hz. The red dashed line marks the separation line.

The surface relative friction drag Fr was spatially averaged over the spanwise range (-25 mm $< z <$ 25 mm), where the separation line exhibits approximately two-dimensional characteristics along the z direction. As shown in Figure 15, both the introduction of MVGs and the oscillation can reduce the surface friction drag. The static configuration yields the

strongest drag reduction. Additionally, oscillation modifies the streamwise position of the maximum friction drag, shifting it from $x = -20$ mm (without MVGs) to $x = -30$ mm (with MVGs). This indicates that MVGs influence not only the flow upstream of the separation region but also the flow within the separation zone. Notably, near the corner ($x = 0$ mm), oil accumulation causes errors in the calculated relative friction drag amplitude, warranting caution when interpreting this region.

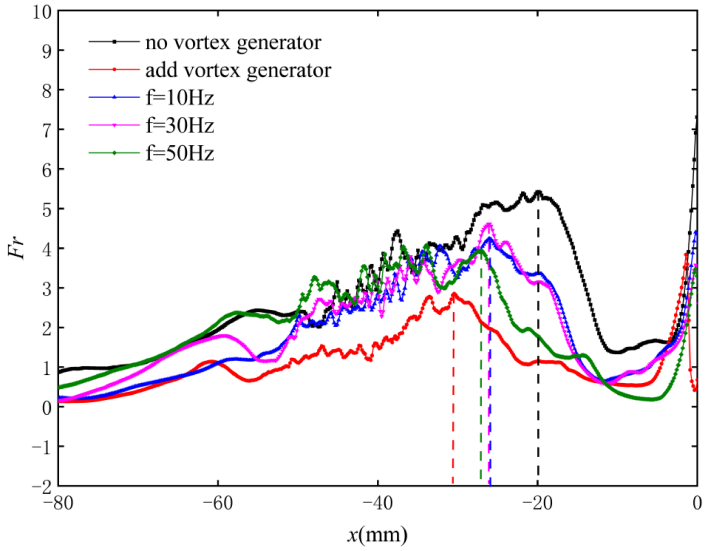

Figure 15. The relative friction along streamwise. The dashed lines mark the streamwise locations of the maximum relative friction.

3.3. Results of High-Speed Schlieren

Figure 16a illustrates part of one snapshot of the Schlieren image to show the instantaneous separation shock. Following the method proposed by [36], the separation shock at a particular wall-normal layer can be detected by locating the streamwise position, where the grayscale intensity abruptly deviates from the mean value before that point, i.e.,

$$P_s \left| I(x,y) = \overline{I}_0(x,y) + \alpha \sigma_{I_0}(x,y) \right. \tag{2}$$

in which $\overline{I}_0(x,y)$ is the mean grayscale intensity upstream the separation shock at the position of (x, y), $\sigma_{I_0(x,y)}$ is the corresponding standard deviation, and the dimensionless coefficient α controls the level of the intensity deviation. Figure 16b illustrates that such a shock detection method can accurately detect the front edge of the separation shock. From the sSchlieren images shown in Figure 16a, the separation shock is observed to occur approximately straight outside the near-wall region of the boundary layer, with the peak pixel grayscale occurring at the shock location (Figure 16b). Accordingly, by fixing a wall-normal height y and analyzing the streamwise grayscale distribution, the streamwise position of the separation shock is identified as the point of maximum grayscale. Repeating this procedure at different wall-normal positions yields a set of discrete points along the separation shock, which are then fitted to a straight line. The intersection of this line with the wall gives the location of the shock foot, and the slope of the line defines the separation shock angle β, both of which are key geometric parameters depicting the unsteady motion of the separation shock.

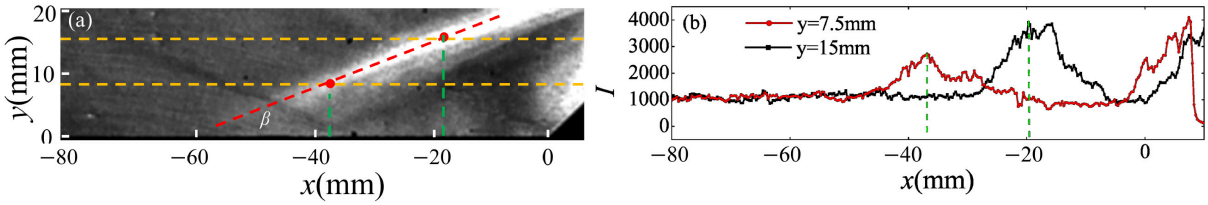

Figure 16. (**a**) One snapshot of an instantaneous Schlieren image; (**b**) the corresponding streamwise profiles of gray intensity I(x) at y = 7.5 mm and y = 15 mm. Yellow dashed: y-position; Green dashed: streamwise location of max. grayscale intensity; Red dashed: separation shock.

A windowed-averaged FFT method was applied to perform a single-point power spectral density analysis of the high-speed Schlieren images. The window type was Gauss-win, with a window duration of 0.05 s and an overlap ratio of 50%. The $St_L = FL/U_\infty$ was used to characterize the shock oscillation characteristics, where F is the low-frequency oscillation frequency of the separation shock, L is the separation zone length, and the freestream velocity U_∞ is taken as the reference velocity. Figure 17 shows the pre-multiplies spectra of the time-series signals of $I(t:x,y)$ at $x = -19$ mm, y = 15 mm on the mean front edge of the separation shock. Due to the limited sampling frequency, spectral information beyond $St_L > 0.25$ is not resolved in the present measurement, but previous studies have shown that the unsteadiness separation shock motion appears in the frequency range of St_L = 0.02–0.05 [37]. Figure 17a presents the low-frequency oscillation spectrum of the separation shock without MVGs, revealing a broadband oscillation within St_L = 0.025–0.055. Upon introducing MVGs and spanwise oscillation (Figure 17b–e), the dominant St_L shifts to approximately 0.04, exhibiting a prominent peak and significantly narrowed bandwidth. This indicates that both static and oscillating MVGs can modulate the low-frequency energy distribution, resulting in an enhancement of the spectral concentration of the shock oscillation. However, the reduced frequency of MVGs is still low compared to the St_L associated with low-frequency shock oscillations, and does not fundamentally change the low-frequency oscillation characteristics of the separation shock.

Schlieren images are further analyzed by POD to obtain a reduced-order representation of the shock motion. Using POD, the fluctuating grayscale intensity field $I'(x,t)$ is decomposed into N discrete POD modes:

$$I'(x,t) = \sum_1^N A_i(t)\Psi_i(x) \tag{3}$$

in which $A_i(t)$ is the time coefficient of the ith POD mode and $\Psi_i(x)$ is the corresponding spatial eigenfunction.

Figure 18((a1)–(d1)) illustrate the pre-multiplied spectra $F\Psi_{A_1}$, $F\Psi_{A_2}$ and spatial eigenfunctions $\Psi_1 \ldots \Psi_2$ with rows from top to bottom corresponding to the cases of no MVGs, added MVGs and spanwise oscillations of 10 Hz, 30 Hz and 50 Hz, respectively. As shown in the left two columns of Figure 18, low-frequency oscillations within the range of 600–1100 Hz are observed, which correspond to the translational motion of the separation shock according to Zhang et al. [38]. The St_L ranges from approximately 0.025 to 0.055, which aligns with the results from single-point POD analysis. The spatial eigenfunction contours shown in the right two columns of Figure 18 indicate a slight upward shift in the time-averaged oscillation position of the shock (displayed by the dashed green line), suggestively indicating that the enlarged separation zone elevates the mean shock oscillation position, consistent with the results obtained by PIV.

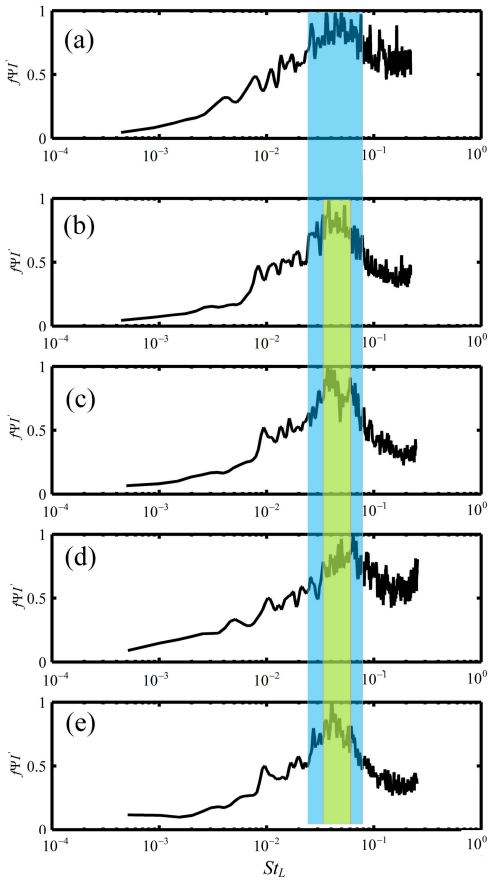

Figure 17. The pre-multiplied spectrum of the separation shock motion: (**a**) no MVGs; (**b**) added MVGs; (**c**) f = 10 Hz; (**d**) f = 30 Hz; (**e**) f = 50 Hz. The blue and yellow boxes denote the St_L ranges of the separation shock without and with vortex generators, respectively.

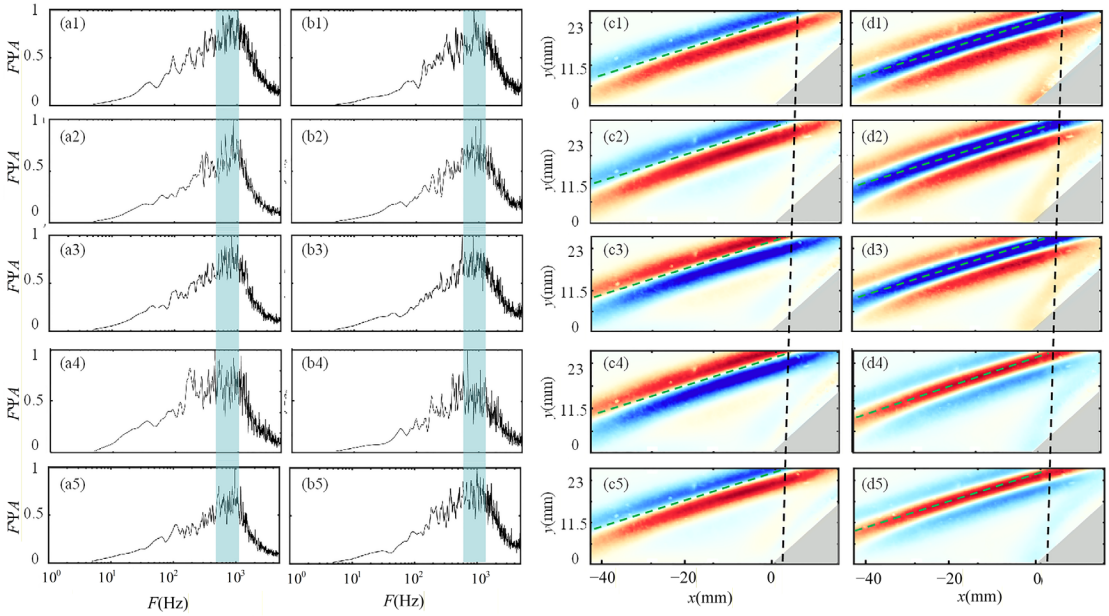

Figure 18. Pre-multiplied spectra $FΨ_{A_1}$ (**a1–a5**), Pre-multiplied spectra $FΨ_{A_2}$ (**b1–b5**), spatial eigenfunctions $Ψ_1$ (**c1–c5**), spatial eigenfunctions $Ψ_2$ (**d1–d5**) for cases with no MVGs, added MVGs, and with MVG oscillating at f = 10 Hz, f = 30Hz, and f = 50 Hz. The blue boxes denote the oscillation ranges of the separation shock. Blue dashed: time-averaged oscillation position of the separation shock; Black dashed: relative positions of the time-averaged separation shock.

4. Conclusions

This paper adopts PIV, high-speed Schlieren photography, and oil-film visualization techniques to capture the spatial and surface flow structures associated with SWBLI over a flat-plate compression ramp. The influence of spanwise oscillation MVGs on SWBLI is systematically examined. Furthermore, through comparative analysis, the characteristics and mechanisms under different conditions are clarified. The main conclusions are summarized as follows.

(1) The introduction and spanwise oscillation of the MVGs do not alter the flow structure within the interaction region. However, they contribute to an increase in boundary layer thickness and shape factor, which leads to an expansion of the absolute separation zone. Notably, due to the three-dimensional nature of the vortex generators, the PIV observations represent the mean features in this plane, and local three-dimensional effects cannot be ruled out.

(2) Compared with the baseline case without MVGs, the fluorescent oil-film measurements reveal relative variations in wall shear stress distributions induced by spanwise oscillation MVGs. The measured relative wall friction remains lower than that of the baseline configuration, and the relative reduction in wall friction gradually diminishes with increasing oscillation frequency.

(3) The St_L of the separation shock ranges approximately from 0.025 to 0.055 in the absence of MVGs. The introduction of MVGs and their spanwise oscillations further modulates the distribution of low-frequency energy, enhancing the oscillation peak and concentrating the St_L around 0.04. Additionally, the MVGs force the separation shock to increase, resulting in a higher time-averaged oscillation position.

Given that the reduced frequency of the vortex generators lies between 0.0007 and 0.0033, compared to the Strouhal number of 0.025–0.055 for the low-frequency shock oscillation in a conventional flat-plate compression ramp, the broadband nature of the shock oscillation is narrowed, but the low-frequency oscillation itself is not effectively suppressed. In future work, the spanwise periodic oscillation frequency of the MVGs could be further increased so that the reduced frequency covers the full range of low-frequency oscillations or reaches the order of the convective time scale of the interaction region, thereby enabling the exploration of forced oscillation control effects on dynamic flow structures and unsteadiness.

Author Contributions: Conceptualization, X.L.; methodology, X.L. and H.W.; validation, X.L.; formal analysis, X.L.; investigation, X.L. and H.W.; resources, X.L. and H.X.; data curation, X.L.; writing—original draft preparation, X.L.; writing—review and editing, X.L.; visualization, X.L., S.R. and H.W.; supervision, X.L. and Z.H.; project administration, H.X. and Z.H.; funding acquisition, X.L. All authors have read and agreed to the published version of the manuscript.

Funding: This research was funded by Qian Xuesen Innovation Fund of China Aerospace Science and Technology Corporation, the Stable support program (800009000199C1772447).

Data Availability Statement: The data are available upon request.

Conflicts of Interest: The authors declare no conflicts of interest.

References

1. Huang, W.; Du, Z.; Yan, L.; Xia, Z. Supersonic mixing in air breathing propulsion systems for hypersonic flights. *Prog. Aerosp. Sci.* **2019**, *109*, 100545.
2. Huang, W.; Du, Z.; Yan, L.; Moradi, R. Flame propagation and stabilization in dual-mode scramjet combustors: A survey. *Prog. Aerosp. Sci.* **2018**, *101*, 13–30. [CrossRef]

3. Huang, W.; Chen, Z.; Yan, L.; Yan, B.; Du, Z. Drag and heat flux reduction mechanism induced by the spike and its combinations in supersonic flows: A review. *Prog. Aerosp. Sci.* **2019**, *105*, 31–39. [CrossRef]
4. Zhu, K.; Jiang, L.; Liu, W.; Sun, M.; Wang, Q.; Hu, Z. Wall temperature effects on shock wave/turbulent boundary layer interaction via direct numerical simulation. *Acta Astronaut.* **2021**, *178*, 499–510. [CrossRef]
5. Schubauer, G.B.; Spangenberg, W.G. Forced mixing in boundary layers. *J. Fluid Mech.* **1960**, *8*, 10–32. [CrossRef]
6. Pearcey, H.H. Shock induced separation and its prevention by design and boundary layer control. *Bound. Layer Flow Control.* **1961**, *2*, 1170–1344.
7. Lin, J.C.; Howard, F.G.; Selby, G.V. Small submerged vortex generators for turbulent flow separation control. *J. Spacecr. Rocket.* **1990**, *27*, 503–507. [CrossRef]
8. Lin, J.C. Control of turbulent boundary-layer separation using micro-vortex generators. In Proceedings of the 30th AIAA Fluid Dynamics Conference, Norfolk, VA, USA, 28 June–1 July 1999.
9. Lin, J.C. Review of research on low-profile vortex generators to control boundary-layer separation. *Prog. Aerosp. Sci.* **2002**, *38*, 389–420.
10. Zhang, Y.; Tan, H.; Wang, Z.; Li, X.; Guo, Y. Progress of shock wave/boundary layer interaction and its control in inlet. *J. Propuls. Technol.* **2020**, *41*, 241–259. (In Chinese)
11. Zhang, B.; Zhao, Q.; Xiang, X.; Xu, J. An improved micro-vortex generator in supersonic flows. *Aerosp. Sci. Technol.* **2015**, *47*, 210–215. [CrossRef]
12. Hristozova, L.; Sebastian, R.; Schreyer, A.M. Flow fields around asymmetrical micro vortex generators in supersonic flow. *Aerosp. Sci. Technol.* **2024**, *145*, 108838.
13. Kaushik, M. Experimental studies on micro-vortex generator controlled shock/boundary layer interactions in Mach 2.2 intake. *Int. J. Aeronaut. Space Sci.* **2019**, *20*, 584–595.
14. Chung, K.-M.; Su, K.-C.; Chang, K.-C. The Effect of Vortex Generators on Shock-Induced Boundary Layer Separation in a Transonic Convex-Corner Flow. *Aerospace* **2021**, *8*, 157.
15. Chidambaranathan, M.; Verma, S.B.; Rathakrishnan, E. Control of incident shock-induced boundary-layer separation using steady micro-jet actuators at M_∞ = 3.5. *Proc. Inst. Mech. Eng. Part G J. Aerosp. Eng.* **2019**, *233*, 095441001774986.
16. Huang, R.; Wang, Z.; Chang, J.; Wang, D.; Hong, Z. The control mechanism of micro-vortex generators on streamwise vortex-shock train coupling interference. *Aerosp. Sci. Technol.* **2025**, *163*, 110308.
17. Verma, S.B.; Manisankar, C. Assessment of various low-profile mechanical vortex generators in controlling a shock-induced separation. *AIAA J.* **2017**, *55*, 2228–2240.
18. Babinsky, H.; Li, Y.; Pitt Ford, C.W. Microramp control of supersonic oblique shock-wave/boundary layer interactions. *AIAA J.* **2009**, *47*, 668–675.
19. Zhang, Y.; Liu, W.; Wang, B.; Sun, M. Effects of micro-ramp on transverse jet in supersonic crossflow. *Acta Astronaut.* **2016**, *127*, 160–170. [CrossRef]
20. Zhao, Y.; Zhang, H.; Zhang, J. Effects of Dynamic Micro Vortex Generator on Shock Wave Boundary Layer Interactions. *J. Propuls. Technol.* **2022**, *43*, 200305.
21. Zhao, Y.; Wu, J.; Zhou, J. Effect of Dynamic Microvortex Generator on SWBLI Based on FD-06 Wind Tunnel. *J. Aerosp. Eng.* **2023**, *36*, 04022106. [CrossRef]
22. Wang, M.; Wang, Z.; Zhang, Y.; Cheng, D.; Tan, H.; Wang, K.; Gao, S. Control of Cowl Shock/Boundary Layer Interaction in Supersonic Inlet Based on Dynamic Vortex Generator. *Aerospace* **2023**, *10*, 729. [CrossRef]
23. Zhang, Y.; Chen, M.; Wang, Z.; Pang, M.; Tan, H.; Zhu, H.; Wang, M. Experimental investigation of the control of shock/boundary layer interaction based on dynamic vortex generator. *Aerosp. Sci. Technol.* **2025**, *162*, 110175. [CrossRef]
24. Junge, W.J.; Mangiavacchi, N.; Akhavan, R. Suppression of turbulence in wall-bounded flows by high frequency spanwise oscillations. *Phys. Fluids A Fluid Dyn.* **1992**, *4*, 1605–1607. [CrossRef]
25. Yao, J.; Hussain, F. Supersonic turbulent boundary layer drag control using spanwise wall oscillation. *J. Fluid Mech.* **2019**, *880*, 388–429. [CrossRef]
26. Sun, D.; Liu, P.; Tong, F. Effect of spanwise oscillation on interaction of shock wave and turbulent boundary layer. *Acta Aeronaut. Astronaut. Sin.* **2020**, *41*, 124054. (In Chinese)
27. Saad, M.R.; Che Idris, A.; Kontis, K. Experimental studies on micro-vortex generators in hypersonic flow. In Proceedings of the 28th Congress of the International Council of the Aeronautical Sciences, Brisbane, Australia, 23–28 September 2012; pp. 1015–1021.
28. Wu, H.; Wang, J.; Huang, W.; Du, Z.; Yan, L. Research progress on shock wave/boundary layer interactions and flow controls induced by micro vortex generators. *Acta Aeronaut. Astronaut. Sin.* **2021**, *42*, 025371.
29. Zhang, Q.; Pan, C.; Wang, J.; Wang, H.; Li, X.; Huang, Z. Tomographic Image Velocimetry Measurement and Reduced-Order Characterization of Hypersonic Compression Ramp Flow. *AIAA J.* **2025**, *63*, 1195–1202. [CrossRef]

30. Yu, J.; Wang, H.; Xiang, X. Unsteady Pressure Measurement of Cavity Flow In a Hypersonic Wind Tunnel Using Fast Response PSP. In Proceedings of the 21st AIAA International Space Planes and Hypersonics Technologies Conference, Xiamen, China, 6–9 March 2017.
31. Samimy, M.; Lele, S.K. Motion of particles with inertia in a compressible free shear layer. *Phys. Fluids A Fluid Dyn.* **1991**, *3*, 1915–1923. [CrossRef]
32. Mfyfr, K.E.; Pedersen, J.M.; Özcan, O. A turbulent jet in crossflow analysed with proper orthogonal decomposition. *J. Fluid Mech.* **2007**, *583*, 199–227. [CrossRef]
33. Horn, B.K.P.; Schunck, B.G. Determining optical flow. *Artif. Intell.* **1981**, *17*, 185–203. [CrossRef]
34. Liu, T.; Shen, L. Fluid flow and optical flow. *J. Fluid Mech.* **2008**, *614*, 253–291. [CrossRef]
35. Liu, T.; Merat, A.; Makhmalbaf, M.H.M.; Fajardo, C.; Merati, P. Comparison between optical flow and cross-correlation methods for extraction of velocity fields from particle images. *Exp. Fluids* **2015**, *56*, 166. [CrossRef]
36. Murugan, J.N.; Govardhan, R.N. Shock wave-boundary layer interaction in supersonic flow over a forward-facing step. *J. Fluid Mech.* **2016**, *807*, 258–302.
37. Clemens, N.T.; Narayanaswamy, V. Low-frequency unsteadiness of shock wave/turbulent boundary layer interactions. *Annu. Rev. Fluid Mech.* **2014**, *46*, 469–492.
38. Zhang, Q.; Pan, C.; Wang, H.; Li, X.; Huang, Z.; Wang, J. Decoupling translation and rotation motion of separation shock in a hypersonic compression ramp flow. *Chin. J. Aeronaut.* **2026**, 104145. [CrossRef]

Disclaimer/Publisher's Note: The statements, opinions and data contained in all publications are solely those of the individual author(s) and contributor(s) and not of MDPI and/or the editor(s). MDPI and/or the editor(s) disclaim responsibility for any injury to people or property resulting from any ideas, methods, instructions or products referred to in the content.